Microswimmer-induced chaotic mixing

Mir Abbas Jalali[1,2,†], **Atefeh Khoshnood**[3] **and Mohammad-Reza Alam**[4]

[1]Department of Astronomy, University of California, Berkeley, CA 94720, USA

[2]Department of Mechanical Engineering, Sharif University of Technology, Azadi Avenue,
P.O. Box 11155-9567, Tehran, Iran

[3]Reservoir Engineering Research Institute, Palo Alto, CA 94301, USA

[4]Department of Mechanical Engineering, University of California, Berkeley, CA 94720, USA

Efficient mixing, typically characterised by chaotic advection, is hard to achieve in low Reynolds number conditions because of the linear nature of the Stokes equation that governs the motion. Here we show that low Reynolds number swimmers moving in quasi-periodic orbits can result in considerable stretching and folding of fluid elements. We accurately follow packets of tracers within the fluid domain and show that their trajectories become chaotic as the swimmer's trajectory densely fills its invariant torus. The mixing process is demonstrated in two dimensions using the Quadroar swimmer that autonomously propels and tumbles along quasi-periodic orbits with multi-loop turning trajectories. We demonstrate and discuss that the streamlines of the flow induced by the Quadroar closely resemble the oscillatory flow field of the green alga *Chlamydomonas reinhardtii*. Our findings can thus be utilized to understand the interactions of microorganisms with their environments, and to design autonomous robotic mixers that can sweep and mix an entire volume of complex geometry containers.

Key words: biological fluid dynamics, mixing, swimming/flying

1. Introduction

Life on the Earth is strongly dependent upon mixing across a vast range of scales. For example, mixing distributes nutrients for microorganisms in aquatic environments (Pushkin & Yeomans 2013), and balances the spatial energy distribution in the oceans and the atmosphere. From an industrial point of view, mixing is essential in many microfluidic processes and lab-on-a-chip operations, polymer engineering, pharmaceutics, food engineering, petroleum engineering and biotechnology (Rauwendaal 1991; Nienow *et al.* 1997; Ottino & Wiggins 2004).

Mixing can be achieved by diffusion, turbulence and stirring. The importance of diffusive over convective mixing is characterised by the Péclet number. In microchannels, the typical value of the Péclet number is usually much larger than $O(1)$ and can easily be of the order of tens of thousands (e.g. Ottino & Wiggins 2004). In the limit of immiscible fluids, the Péclet number is infinity, pointing to the inefficiency of diffusion for mixing in most lab-on-a-chip devices. Although turbulence is an efficient mixing mechanism, generating turbulence in a flow whose

† Email address for correspondence: mjalali@berkeley.edu

Reynolds number is naturally very low (i.e. flow of highly viscous fluids) is typically very energy intensive, especially for applications in which long-chain molecules cannot be strained arbitrarily and must be treated with extreme care (Aref 1991). As a result, in many low Reynolds number applications active stirring, implemented through creating a relative speed between the fluid and an object, is the preferred mixing strategy (Nienow *et al.* 1997; Mathew *et al.* 2007; Couchman & Kerrigan 2010).

The most efficient form of mixing is chaotic mixing (Ottino 1989, 1990; Wiggins & Ottino 2004). If the fluid flows inside a channel (e.g. flow in microchannels), the channel geometry or carvings on the channel wall can be architected to result in chaotic mixing as the flow passes (e.g. Liu *et al.* 2000; Stroock *et al.* 2002). Forced mixing protocols have also been introduced for mixing in closed vessels (Gouillart *et al.* 2007, 2008). A rod moving on a periodic eight shaped path can homogenize the concentration of a low-diffusivity dye in a vessel whose boundaries are close enough to the path of the moving rod. The mixing efficiency depends on the wall conditions (Sturman & Springham 2013), and is enhanced in the presence of moving walls (Thiffeault *et al.* 2011). The wall effect in the moving rod experiment is pronounced because in a zeroth-order model, the rod behaves like a point force and the induced velocity field is a Stokeslet that has the shallow declining profile $\sim r^{-1}$, with r measuring the distance from the axis of the rod.

Of primary interest for this work is stirring, and the consequent mixing, induced by the motility of microorganisms and microswimmers. This type of mixing has been extensively investigated both computationally and experimentally, characterised by the enhanced effective diffusivity (Wu & Libchaber 2000; Lin, Thiffeault & Childress 2011; Eckhardt & Zammert 2012; Pushkin & Yeomans 2013; Wagner *et al.* 2014). The concept of stirring highly viscous fluids by use of low Reynolds number swimmers is different from protocols with moving forces because the resultant force exerted by a swimmer on its environmental fluid is zero, and the leading term in the velocity field is a Stokes dipole that steeply drops as $\sim r^{-2}$ (e.g. Pak & Lauga 2015). Consequently, the wall effect becomes weaker and a swimmer can only stir its close proximity, but without wasting too much energy to overwhelm viscous dissipation by the boundaries. Mixing a large volume of fluid is therefore possible either when the number of swimmers is large, or when a single swimmer sweeps a large area or volume. Here, we are interested in mixing by a single swimmer that can access remote regions and containers with complex geometries.

We report the first demonstration of chaotic mixing induced by a microswimmer that strokes on quasi-periodic orbits with multi-loop turning paths. We introduce the geometry of the swimmer in §2 and derive its governing equations of motion. Hydrodynamic interactions between rotating actuators are taken into account in our analysis. The mechanism of mixing is demonstrated in §4 by following a fluid patch marked by tracer particles, and the existence of chaos is proved using finite-time Lyapunov exponents. Applications of microswimmer-induced mixing and future prospects are discussed in §5.

2. The swimmer and equations of motion

We consider a recently proposed swimmer, the Quadroar (Jalali, Alam & Mousavi 2014), which is composed of four rotating disks of radius a at the ends of its two axles, and a chassis of variable length. Each axle has a length of $2b$ and the length of the chassis $2l + 2s(t)$ is varied by a linear actuator (figure 1a). The chassis and axles make an I-shape planar frame. A body-fixed coordinate system (x_1, x_2, x_3) with the
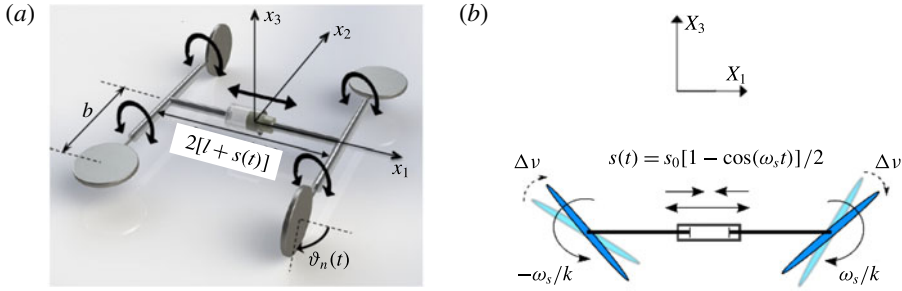
FIGURE 1. (Colour online) (*a*) The geometry of the Quadroar. The centre of the body-fixed coordinate system (x_1, x_2, x_3) is at the centre of mass of the swimmer. (*b*) The geometry of the swimmer as seen along the positive x_2-axis, which is parallel to the axles. The chassis performs its open $\rightleftarrows$ close function according to a harmonic function with a constant frequency ω_s. The front and rear disks counter-rotate with the base angular velocities $\dot\vartheta_1 = \dot\vartheta_2 = \omega_s/2$ and $\dot\vartheta_3 = \dot\vartheta_4 = -\omega_s/2$, respectively, but their rotational frequencies can be shifted by $\Delta\nu_n$.

unit base vectors (e_1, e_2, e_3) is chosen to describe the kinematics and dynamics of the swimmer's translational and rotational movements. The x_1-axis is along the chassis, the x_2-axis is parallel to the axles and the x_3-axis is normal to the plane of the I-frame. The relative orientation of the nth disk with respect to the swimmer's frame is measured by the angle $-\pi \leqslant \vartheta_n \leqslant +\pi$ that the plane of the disk makes with the (x_1, x_2) coordinate plane. We define the global coordinate frame (X_1, X_2, X_3) with the unit base vectors (E_1, E_2, E_3), and denote the position vector of the swimmer's centre of mass by $X_c(t)$. The translational velocity of the swimmer thus becomes $v_c = \dot X_c$. Here, an overdot stands for d/dt. We will represent all physical quantities in terms of the unit vectors e_i in the body-fixed coordinate frame, and will explicitly state if we switch to the global coordinate system.

The main difference between the Quadroar and other swimmer designs such as those that use linked spheres is the point torque that each rotating disk of the Quadroar exerts on the background fluid. Consequently, the streaming of the background fluid in response to the combined translational and rotational motions of the disks (propellers) is a combination of Stokeslets and rotlets. Jalali *et al.* (2014) ignored the hydrodynamic interactions between the disks of the swimmer by assuming that they are sufficiently far from each other. Since this study is going to address the near and far flow fields generated by the swimmer, hydrodynamic interactions of the four disks cannot be ignored. We thus derive new equations of motion for the swimming of the Quadroar taking full account of hydrodynamic interactions. Nonetheless, we retain one of our basic simplifying assumptions: each disk interacts with the background fluid through a point force and a point torque, both applied at the centre of the disk. Therefore, in our analysis, the disks still need to be far from each other such that geometrical effects on streamlines due to the 'finite sizes' of the disks can be ignored.

The Quadroar can propel both in stepwise and continuous operation modes. In this study, we consider continuous operation modes that result in two-dimensional orbits of the swimmer in its sagittal (x_1, x_3)-plane. In the operation mode that we are interested in, the chassis expands and contracts according to the harmonic function $s(t) = s_0[1 - \cos(\omega_s t)]/2$, and the front and rear disks counter-rotate with the base

frequency $\omega_s/2$ (figure 1b). Our control input is the small frequency shift $\Delta\nu$ that detunes the rotational speeds of the front and rear disks as

$$\vartheta_1 = \vartheta_2 = \omega_s/2, \quad \vartheta_3 = \vartheta_4 = -\omega_s/2 + \Delta\nu. \tag{2.1a,b}$$

The swimming dynamics is therefore associated with two time scales: the fast time $T_{fast} = 2\pi/\omega_s$ and the slow time $T_{slow} = 2\pi/\Delta\nu$. Jalali *et al.* (2014) showed that the Quadroar strokes rectilinearly along its x_3 body axis for $\Delta\nu = 0$, and swims on quasi-periodic orbits for non-zero frequency shifts. While depending on the geometrical aspects of the Quadroar details of trajectories maybe different, quasi-periodic orbits also exist when hydrodynamic interactions between disks are included. Quasi-periodic orbits have remarkable consequences on the streaming of the background fluid, which we explore here.

The relative position vector of the nth disk with respect to the centre of mass of the swimmer is defined by $\boldsymbol{r}_n$. We have

$$\boldsymbol{r}_1 = [l + s(t)]\boldsymbol{e}_1 + b\boldsymbol{e}_2, \quad \boldsymbol{r}_3 = -[l + s(t)]\boldsymbol{e}_1 + b\boldsymbol{e}_2, \tag{2.2a,b}$$

$$\boldsymbol{r}_2 = [l + s(t)]\boldsymbol{e}_1 - b\boldsymbol{e}_2, \quad \boldsymbol{r}_4 = -[l + s(t)]\boldsymbol{e}_1 - b\boldsymbol{e}_2. \tag{2.2c,d}$$

Due to the expanding and contracting motion of the chassis (body link), each disk of the Quadroar has a relative velocity $\boldsymbol{v}_{rel,n}$ with respect to the centre of mass. The relative velocities are computed by taking the time derivatives of $\boldsymbol{r}_n$ in the body-fixed coordinate system. For the front disks ($n = 1, 2$) and rear disks ($n = 3, 4$) one has $\boldsymbol{v}_{rel,1} = \boldsymbol{v}_{rel,2} = \dot{s}\boldsymbol{e}_1$ and $\boldsymbol{v}_{rel,3} = \boldsymbol{v}_{rel,4} = -\dot{s}\boldsymbol{e}_1$, respectively. Here $\dot{s}$ is the expansion or contraction rate of the chassis.

The angular velocity of the swimmer, which is also the angular velocity of the body-fixed coordinate system, is denoted by $\boldsymbol{\omega}_{body}(t)$. It is related to the 1-2-3 sequence of Euler angles $\boldsymbol{\alpha} = (\phi, \theta, \psi)$ through the following transformation

$$\boldsymbol{\omega}_{body} = \boldsymbol{T} \cdot \dot{\boldsymbol{\alpha}}, \quad \boldsymbol{T} = \begin{bmatrix} 1 & 0 & -s_\theta \\ 0 & c_\phi & c_\theta s_\phi \\ 0 & -s_\phi & c_\theta c_\phi \end{bmatrix}, \tag{2.3a,b}$$

where s_γ and c_γ denote $\sin(\gamma)$ and $\cos(\gamma)$, respectively. The transformation between body-fixed and global coordinate systems is carried out using the rotation matrix

$$\boldsymbol{R} = \boldsymbol{R}_{x_1}\boldsymbol{R}_{x_2}\boldsymbol{R}_{x_3} = \begin{bmatrix} 1 & 0 & 0 \\ 0 & c_\phi & s_\phi \\ 0 & -s_\phi & c_\phi \end{bmatrix} \begin{bmatrix} c_\theta & 0 & -s_\theta \\ 0 & 1 & 0 \\ s_\theta & 0 & c_\theta \end{bmatrix} \begin{bmatrix} c_\psi & s_\psi & 0 \\ -s_\psi & c_\psi & 0 \\ 0 & 0 & 1 \end{bmatrix}. \tag{2.4}$$

For instance, the velocity of the centre of mass in the body-fixed coordinate system reads $\boldsymbol{R} \cdot \dot{\boldsymbol{X}}_c$. The absolute linear and angular velocities of the nth disk are thus determined from

$$\boldsymbol{v}_n = \boldsymbol{v}_c + \boldsymbol{v}_{rel,n} + \boldsymbol{\omega}_{body} \times \boldsymbol{r}_n, \tag{2.5}$$

$$\boldsymbol{\omega}_n = \boldsymbol{\omega}_{body} + \dot{\vartheta}_n \boldsymbol{e}_2. \tag{2.6}$$

We define the isotropic tensor $\boldsymbol{G} = (32/3)a^3\boldsymbol{I}$, with $\boldsymbol{I}$ being the identity matrix and the translation matrix (Jalali *et al.* 2014)

$$\boldsymbol{K}_n = \frac{8}{3}a \begin{bmatrix} 5 - \cos(2\vartheta_n) & 0 & \sin(2\vartheta_n) \\ 0 & 4 & 0 \\ \sin(2\vartheta_n) & 0 & 5 + \cos(2\vartheta_n) \end{bmatrix}. \tag{2.7}$$

At its hydrodynamic centre, the nth disk exerts the force vector $\boldsymbol{f}_n$ and torque $\boldsymbol{\tau}_n$ on the fluid. The reactions of these are the drag forces and torques. Within a non-inertial streaming fluid, the following analytic expressions are known (Happel & Brenner 1983)

$$\boldsymbol{f}_n = \mu \boldsymbol{K}_n \cdot (\boldsymbol{v}_n - \boldsymbol{u}_n), \quad \boldsymbol{\tau}_n = \mu \boldsymbol{G} \cdot (\boldsymbol{\omega}_n - \boldsymbol{\Omega}_n), \tag{2.8a,b}$$

where $\boldsymbol{u}(X, t)$ and $2\boldsymbol{\Omega}(X, t) = \nabla \times \boldsymbol{u}$ are the streaming and vorticity fields of the background fluid with the dynamic viscosity μ, and we have

$$\boldsymbol{u}_n = \boldsymbol{u}(X_c + \boldsymbol{r}_n, t), \quad \boldsymbol{\Omega}_n = \boldsymbol{\Omega}(X_c + \boldsymbol{r}_n, t). \tag{2.9a,b}$$

It is noted that the drag forces and torques occur when the relative linear and angular velocities within the parentheses in (2.8a,b) are non-zero. The effects of $\boldsymbol{u}_n$ and $\boldsymbol{\Omega}_n$ cannot be neglected for compact swimmers whose own propellers are close to each other and have hydrodynamic interactions.

For a neutrally buoyant swimmer in low Reynolds number conditions, $Re \to 0$, the drag force and torque vanish and we obtain

$$\text{force balance:} \quad \sum_{n=1}^{4} \boldsymbol{f}_n = \boldsymbol{0}, \tag{2.10}$$

$$\text{torque balance:} \quad \sum_{n=1}^{4} (\boldsymbol{r}_n \times \boldsymbol{f}_n + \boldsymbol{\tau}_n) = \boldsymbol{0}. \tag{2.11}$$

These equations are still incomplete for the determination of the translational and rotational dynamics of the swimmer as they contain the unknown velocities $\boldsymbol{u}_n$ and spins $\boldsymbol{\Omega}_n$ that are developed in the background fluid because of the activity of the swimmer itself: each disk generates a flow and influences the operation of other propellers. If we assume that the kth disk exerts a point force and torque (at its hydrodynamic centre) on the fluid, the velocity field that it generates at X will be the combination of a Stokeslet and a rotlet as (e.g. Lopez & Lauga 2014)

$$\boldsymbol{U}_k(X, t) = \frac{\boldsymbol{f}_k}{z} + \frac{(\boldsymbol{f}_k \cdot X)}{z^3} X + \frac{\boldsymbol{\tau}_k \times X}{z^3}, \quad z = (X \cdot X)^{1/2}. \tag{2.12}$$

Operating (2.12) with $\nabla \times$ gives the vorticity field:

$$\boldsymbol{\xi}_k(X, t) = \frac{2\boldsymbol{f}_k \times X}{z^3} + \frac{3(\boldsymbol{\tau}_k \cdot X)X - z^2 \boldsymbol{\tau}_k}{z^5}. \tag{2.13}$$

The velocity and vorticity fields induced at the hydrodynamic centre of the nth disk by three other disks are thus determined from

$$\boldsymbol{u}_n = \sum_{\substack{k=1 \\ k \neq n}}^{4} \left[\frac{\boldsymbol{f}_k}{z_{kn}} + \frac{(\boldsymbol{f}_k \cdot X_{kn})}{z_{kn}^3} X_{kn} + \frac{\boldsymbol{\tau}_k \times X_{kn}}{z_{kn}^3} \right], \tag{2.14}$$

$$2\boldsymbol{\Omega}_n = \sum_{\substack{k=1 \\ k \neq n}}^{4} \left[\frac{2\boldsymbol{f}_k \times X_{kn}}{z_{kn}^3} + \frac{3(\boldsymbol{\tau}_k \cdot X_{kn})X_{kn} - z_{kn}^2 \boldsymbol{\tau}_k}{z_{kn}^5} \right], \tag{2.15}$$

where $X_{kn} = r_n - r_k$ and $z_{kn} = (X_{kn} \cdot X_{kn})^{1/2}$. In these equations, the forces f_k and torques τ_k linearly depend on u_k and Ω_k through relations in (2.8a,b). We collect the 30 unknown components of the vectors v_c, ω_{body}, u_n and Ω_n ($n = 1, 2, 3, 4$) in the vector w, and combine (2.14) and (2.15) with (2.10) and (2.11) to obtain a system of linear equations

$$L(v_c, \omega_{body}, u_1, \ldots, u_4, \Omega_1, \ldots, \Omega_4, t) = L(w, t) = 0, \qquad (2.16)$$

in terms of w and t, with L being a vectorial function of dimension 30×1. We then analytically calculate the Jacobian of L and transform (2.16) to

$$A(t) \cdot w = d(t) \equiv L|_{w=0}, \quad A(t) = \left[\frac{\partial L}{\partial w}\right]_{30 \times 30}. \qquad (2.17)$$

Here the matrix $A(t)$ and the right-hand side vector $d(t)$ explicitly depend on t through the control variables $s(t)$ and $\vartheta_n(t)$. At each time step, the linear system of (2.17) is solved using a standard LU decomposition method with pivoting. After calculating v_c and ω_{body}, the position vector $X_c = X_{c,i} E_i$ and orientation angles of the swimmer are found by the direct numerical integration of

$$\dot{X}_c = R^{\mathrm{T}} \cdot v_c, \quad \dot{\alpha} = T^{-1} \cdot \omega_{body}, \qquad (2.18a,b)$$

with the superscript T denoting transpose. We now express all physical quantities in terms of the unit vectors E_i of the global coordinate system. This is simply done by left-multiplying all vectors in the (x_1, x_2, x_3) frame by R^{T}. The flow field generated by the Quadroar is a superposition of the Stokeslets and rotlets of the four disks:

$$u(X, t) = u_i E_i = \sum_{n=1}^{4} \left[\frac{f_n}{z_n} + \frac{(f_n \cdot X_n)}{z_n^3} X_n + \frac{\tau_n \times X_n}{z_n^3}\right], \quad z_n = (X_n \cdot X_n)^{1/2}, \quad (2.19)$$

$$X_n = X - X_c(t) - r_n(t), \qquad (2.20)$$

where f_n and τ_n are computed using the components of $w(t)$. We study the flow characteristics by following the Lagrangian trajectories of passive tracers. The equation of motion for a tracer becomes

$$\frac{\mathrm{d}X}{\mathrm{d}t} = u(X, t), \qquad (2.21)$$

which is integrated in the global coordinate system simultaneous with the swimmer's equations of motion in (2.18a,b). Due to the coupled rotational and translational motions of the swimmer and their effect on the background fluid and tracers, the equations of motion are highly nonlinear and we need an accurate integrator to avoid spurious mixing due to numerical errors. Leap frog integrators devised for second-order ordinary differential equations do not work well here because we do not have evolution equations for the velocities – there is no acceleration in the low Reynolds flow regimes. We therefore adopt the RK78 integrator (Fehlberg 1968) that can keep relative integration errors at $O(10^{-14})$ over long time scales that a quasi-periodic orbit becomes dense in its invariant manifold or chaotic orbits uniformly sample their invariant measure.
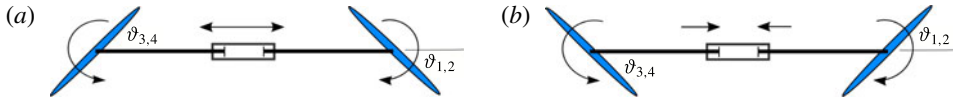
FIGURE 2. (Colour online) Side views of the Quadroar swimmer during a rectilinear motion: the front and rear disks counter-rotate with the same angular velocities, and their inclinations with respect to the chassis are identical but with different signs. (*a*) and (*b*) respectively show the swimmer's conformations during the expansion ($\dot{s} > 0$) and contraction ($\dot{s} < 0$) phases of the chassis.

3. Flow field

The Quadroar is a three-dimensional swimmer with rich orbital structure in the phase space. Nonetheless, to study the quantitative and qualitative effects of swimming on environmental fluid, and gain insight into the regions of influence of microswimmers, we investigate two-dimensional quasi-periodic motions in the body-fixed (x_1, x_3) coordinate system. The parameters of our model swimmer have been set to $a = 1$, $b = 4$, $l = 4$, $\omega_s = 1$, and $s_0/l = 1/2$. We assume that all disks start their rotations in phase, $\vartheta_n = 0$ ($n = 1, 2, 3, 4$), and the initial conditions for the position and orientation of the swimmer are set to $\boldsymbol{X}_c = \boldsymbol{0}$ and $\boldsymbol{\alpha} = \boldsymbol{0}$. Depending on our choice of the control parameter $\Delta\nu$ in (2.1*a,b*), the swimmer can take different courses of quasi-periodic orbits.

The simplest motion is rectilinear with $\Delta\nu = 0$: the front and rear disks counter-rotate as the chassis periodically expands and contracts. Disks simultaneously become parallel and perpendicular to the swimmer's body plane (x_1, x_2) at the times $t = j\,T_{fast}$ and $t = (2j + 1)T_{fast}/2$ ($j = 0, 1, 2, \ldots$), respectively. When the chassis is expanding, $\dot{s} > 0$, the inclination angles of the front and rear disks (with respect to the swimmer's body plane) vary in the intervals $0 \leqslant \vartheta_1 = \vartheta_2 \leqslant \pi/2$ and $-\pi/2 \leqslant \vartheta_3 = \vartheta_4 \leqslant 0$, respectively. In such conditions, the swimmer has the conformation of figure 2(*a*). During the contraction phase of the chassis, $\dot{s} < 0$, the front and rear disks respectively evolve in the intervals $\pi/2 \leqslant \vartheta_1 = \vartheta_2 \leqslant \pi$ and $-\pi \leqslant \vartheta_3 = \vartheta_4 \leqslant -\pi/2$ and the swimmer has the conformation of figure 2(*b*). We have used (2.19) to compute the flow field $\boldsymbol{u}(\boldsymbol{X}, t)$ induced by the swimmer. Streamlines and velocity vectors have been displayed in figure 3 for several values of $0 < t < T_{fast}$ during a full cycle of the swimmer's stroke. Since there is no net motion/flow in the x_2 direction, we have visualised $\boldsymbol{u}$ only in the (X_1, X_3) slice of the configuration space that overlaps with the (x_1, x_3) coordinate plane. Another justification for selecting the (X_1, X_3) plane is to avoid the geometrical effects of the disks, which have finite sizes: our methodology of modelling the disks by $\boldsymbol{f}_k$ and $\boldsymbol{\tau}_k$ is supposed to give reasonable results for $\boldsymbol{u}$ if $|\boldsymbol{X} - \boldsymbol{X}_c - \boldsymbol{r}_n| \gg a$. This condition is fulfilled in the (x_1, x_3) plane.

Each stroke cycle begins with the expansion of the chassis and two lateral vortices are formed on the anterior side of the swimmer. These two vortices are pushed forward and shrink in size as the inclination angles ϑ_n increase (figure 3*a,b*). For $|\vartheta_n| \approx \pi/4$, the lateral vortices disappear and the flow field takes a hyperbolic structure where the fluid is pumped in towards the centre of mass of the swimmer along the X_3-axis, and is pumped out along the X_1-axis (figure 3*c*). During this transitional phase, the swimmer behaves like a puller dipole swimmer (e.g. Elgeti, Winkler & Gompper 2015). As the disks make right angles with respect to the chassis, two counter-rotating side vortices are generated by the disks (figure 3*d*). When the chassis contracts, the swimmer behaves like a pusher dipole: the fluid is pumped in along
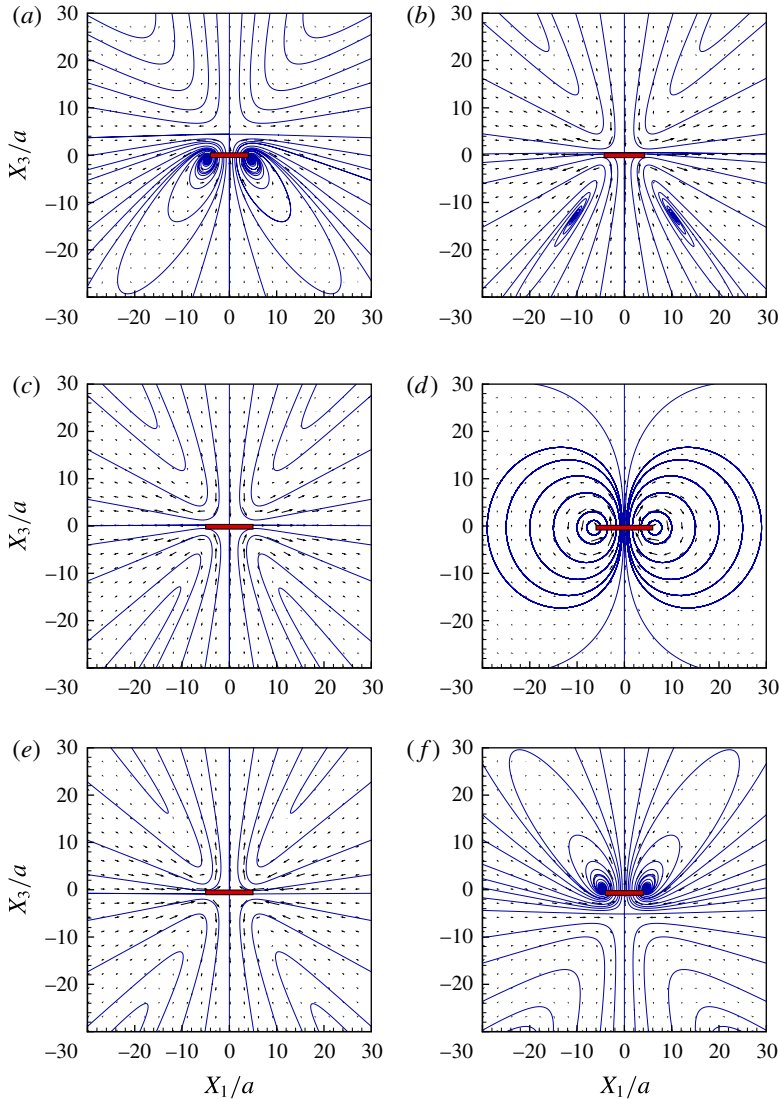
FIGURE 3. (Colour online) Snapshots of the streamlines of the flow field $u(X, t)$ induced by the Quadroar swimmer that starts its motion form $(X_1, X_3) = (0, 0)$ and strokes along the negative X_3-axis. The chassis of the swimmer with variable length $2l + 2s(t)$ has been shown by a thick red bar. For each panel, the conformation of the swimmer's disks can be determined in terms of sign($\dot{s}$) and figure 2. The inclinations of the disks with respect to the swimmer's chassis can be computed using the following equations: $\vartheta_1 = \vartheta_2 = \omega_s t/2$ and $\vartheta_3 = \vartheta_4 = -\omega_s t/2$. (a) $t = (1/64)T_{fast}$, $\dot{s} > 0$, (b) $t = (8/64)T_{fast}$, $\dot{s} > 0$, (c) $t = (16/64)T_{fast}$, $\dot{s} > 0$, (d) $t = (32/64)T_{fast}$, $\dot{s} = 0$, (e) $t = (48/64)T_{fast}$, $\dot{s} < 0$, (f) $t = (63/64)T_{fast}$, $\dot{s} < 0$.

the X_1-axis and pumped out along the X_3-axis as in pushers (figure 3e). The flow structure is hyperbolic for $|\vartheta_n| \approx \pi/4$, and lateral vortices occur behind the swimmer for smaller inclinations of the disks (figure 3f). The Quadroar is therefore a hybrid swimmer that inherits the features of both pusher and puller dipole swimmers. The
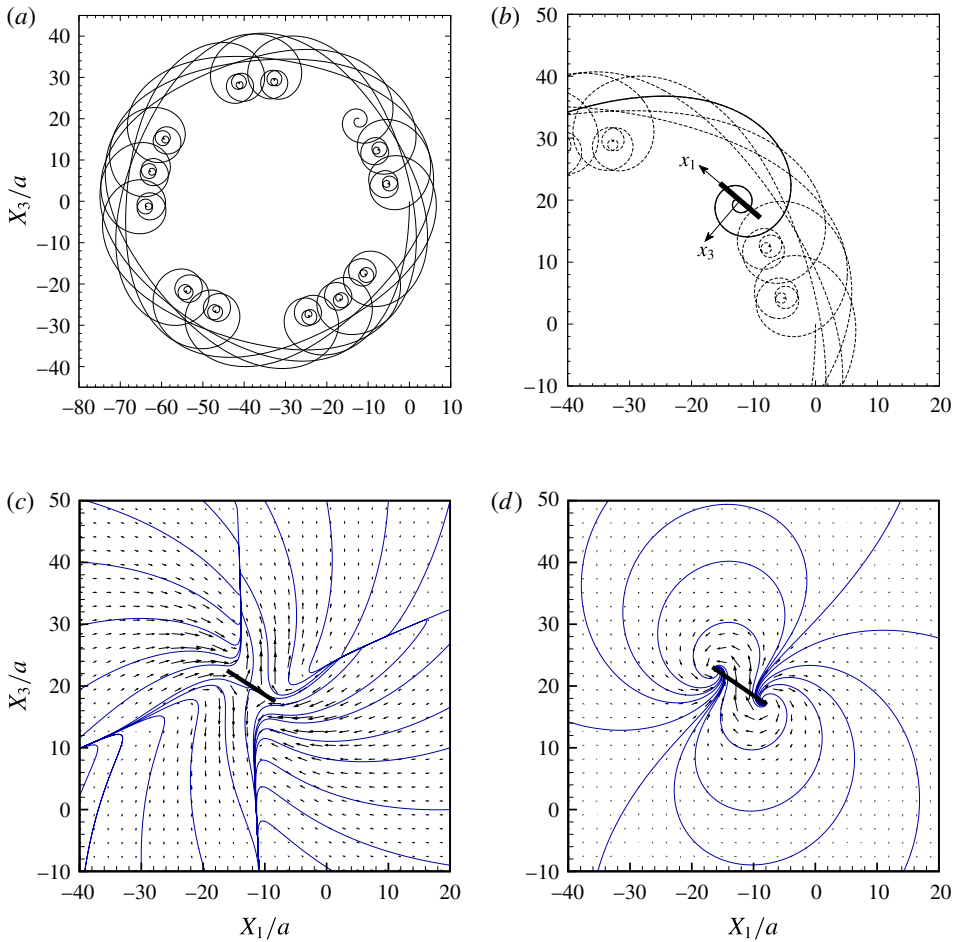
FIGURE 4. (Colour online) (*a*) The quasi-periodic orbit of the swimmer integrated from $(X_1, X_3) = (0, 0)$ over the time interval $0 \leqslant t \leqslant t_{max} = 6.25T_{slow}$. The orbit precesses and becomes dense in an annular region. (*b*) A close-up snapshot of the orbit near the swimmer's position at t_{max}. The orientation of the body-fixed coordinate frame (x_1, x_3) is displayed at t_{max}. (*c*) The streamlines and local velocity vectors of the flow field $\boldsymbol{u}(\boldsymbol{X}, t)$ at $t = 6.25T_{slow} - (7/8)T_{fast}$. (*d*) Same as (*c*) but for $t = 6.25T_{slow} - (3/4)T_{fast}$. The thick bar shows the chassis of the swimmer.

streamlines displayed in figure 3 resemble the oscillatory flow field of a single-celled swimming alga called *C. reinhardtii* (Guasto, Johnson & Gollub 2010).

4. Chaotic mixing

The rectilinear mode of swimming helps us gain insight into the flow physics around microswimmers, but it is not useful for mixing due to two obvious reasons: (i) a rectilinear trajectory has measure zero in the two-dimensional configuration space, and (ii) fluid particles affected by a distant swimmer passing on a straight line move on loop-like paths (Pushkin & Yeomans 2013), which are not effective in the stirring of environmental fluid. We therefore turn our attention to curved quasi-periodic orbits of non-zero measure. We set $\Delta v = 0.00125$ that generates the precessing orbit of figure 4(*a*) for the swimmer's centre of mass. The trajectory has

inverted multi-loop turns aligned towards the centre of the orbit and becomes dense in an annular region $\mathscr{A}$, which is the projection of a three-dimensional torus $\mathscr{M}$ in the (X_1, X_3, θ)-space on the (X_1, X_3)-plane. In the literature of dynamical systems theory, $\mathscr{M}$ is called the 'invariant torus' of a quasi-periodic orbit. We have integrated the equations of motion from $t = 0$ to $t_{max} = 6.25T_{slow}$. Figure 4(*b*) shows a close-up of the trajectory and highlights it over the time interval $6.03T_{slow} \leqslant t \leqslant t_{max}$. We have also shown in this figure the location and orientation of the swimmer's chassis and its body-fixed coordinate system at t_{max}.

Near the state of the swimmer shown in figure 4(*b*), we have plotted the streamlines and local velocity vectors at the two instants $t = 6.25T_{slow} - (7/8)T_{fast}$ (figure 4*c*) and $t = 6.25T_{slow} - (3/4)T_{fast}$ (figure 4*d*). We have only shown the velocity field in the (x_1, x_3) body plane that passes through the centre of mass of the swimmer and overlaps with the global (X_1, X_3) plane. It can be seen how the swimmer pumps the fluid while making a spiral turn. Here the magnitudes of $\vartheta_{1,2}$ and $\vartheta_{3,4}$ differ due to gradual phase shift generated by $\Delta \nu$, and streamlines are rapidly evolving. The twisted hyperbolic structure of figure 4(*c*) occurs when the swimmer strokes like a puller dipole, and four separatrices intersect at a saddle node which is close to the swimmer's centre of mass. The flow stream of figure 4(*d*) originates around one axle and sinks towards the other one. This pattern has no analog in rectilinear motion and is a consequence of phase shift between front and rear disks and spiralling motion. These patterns are few demonstrative examples which show how a swimmer moving on a curved path induces complex, evolving topologies of streamlines. Depending on the phase shift $\vartheta_{1,2} + \vartheta_{3,4} = \Delta \nu\, t$, the swimmer's trajectory and its orientation, new topologies can emerge.

To understand the mixing process and its efficiency, we follow the Lagrangian trajectories of a packet of tracers as the orbit of the swimmer illustrated in figure 4(*a*) becomes dense in the annular region $\mathscr{A}$. We choose a uniformly distributed set of 2500 passive tracers in the rectangular region $\mathscr{D}_0 = \{(X_1, X_3)| -70 \leqslant X_1 \leqslant -67.5,\ -1.25 \leqslant X_3 \leqslant 1.25\}$, which lies well in the ring of the swimmer's orbit. To visualise the mixing process and deformation of fluid elements, we split $\mathscr{D}_0$ to four equal square subdomains and tag their corresponding tracers in a clockwise order by filled blue, green, black and red dots (figure 5*a*). We then release the swimmer from $(X_1, X_3) = (0, 0)$ and integrate (2.18*a*,*b*) for the swimmer and (2.21) for the tracers. The fluid element $\mathscr{D}_0$ starts to deform and is mapped to the set $\mathscr{D}(t)$ as the time elapses. Figure 5(*a*) demonstrates the shape of $\mathscr{D}(t)$, with $\mathscr{D}(0) = \mathscr{D}_0$, at four snapshots in time. It is seen that the fluid element and the contact lines between its four subdomains are deformed gradually from $t = 0$ to $t = 6.25T_{slow}$ but the element keeps its integrity.

The element is highly stretched and folded later at $t = 10T_{slow}$ and starts to develop tails. Over this period, the swimmer has completed approximately 21 turning loops of its quasi-periodic orbit. The folded patch evolves to thin wavy structures as seen in figure 5(*b*) and the contact lines between the four subdomains are destroyed, allowing tracers to gradually distance from their associates. The set $\mathscr{D}(t)$ shown in figure 5(*c*) at $t = 50T_{slow}$ no longer exhibits the properties of a manifold and is topologically similar to strange attractors of dissipative dynamical systems, although it is just an intermediary and not a final stage of an ongoing mixing process. The swimmer completely disperses tracers in $\mathscr{A}$ as $t \to \infty$. The tracers of the four subdomains of $\mathscr{D}_0$ have been well mixed by $t = 125T_{slow}$ (figure 5*d*).
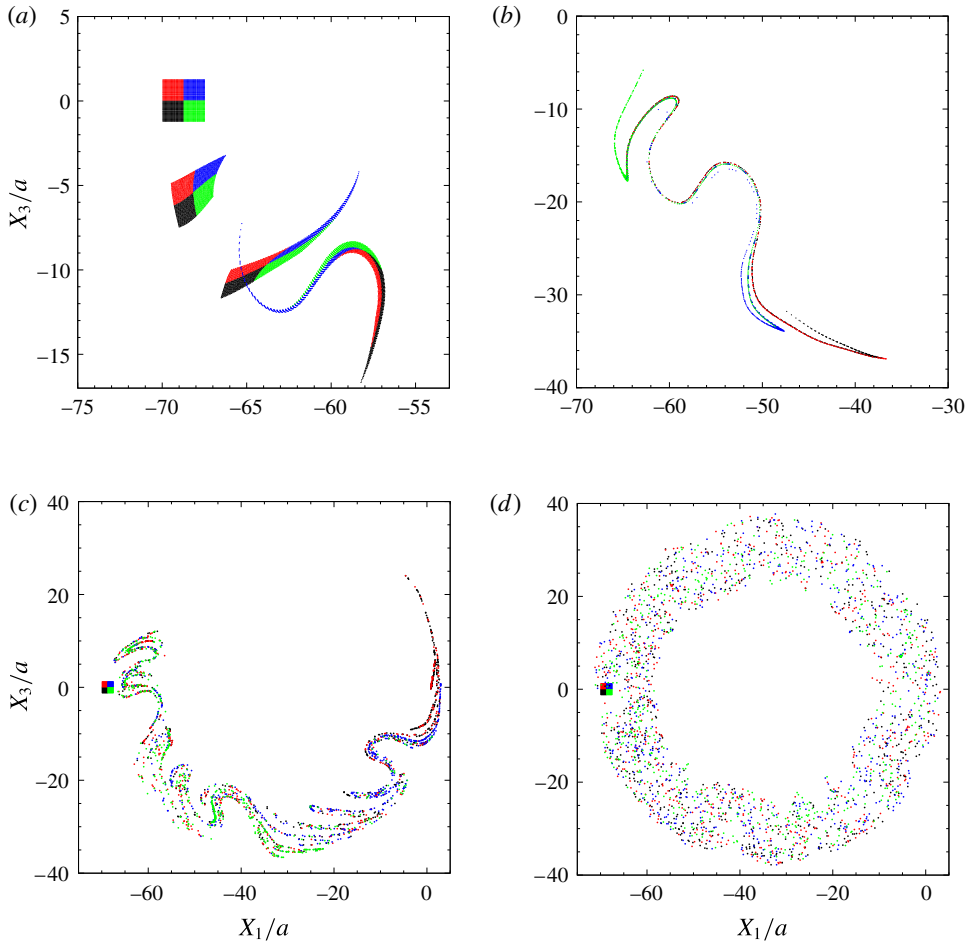
FIGURE 5. (Colour online) Dispersion of a packet of passive tracers by a single quasi-periodic orbit swimmer. The packet has been split to four subdomains of different colours. (*a*) The initial condition of the packet, and its subsequent states at $t/T_{slow} = 3.75$, 6.25 and 10 where $T_{slow} = 2\pi/\Delta\nu$. The packet is folded and stretched in the flow field of the swimmer of figure 4. (*b*) A highly folded and stretched intermediary state of the patch at $t = 22.5T_{slow}$. Contact lines between four subdomains are being destroyed: (*c*) $t = 50T_{slow}$. The contact lines between the four subdomains of the initial patch have been completely destroyed and the mixing process has started. (*d*) The fully mixed state of the patch at $t = 125T_{slow}$. Tracers have been dispersed uniformly within the annular region $\mathscr{A}$ filled by the swimmer's orbit. The initial packet is also superimposed in panels (*c*) and (*d*) for comparison. Note the different scales of panels.

Various measures can be utilized to quantify the mixing process, including entropy, Lyapunov exponents and the mix-norm of advected scalar fields by chaotic flows (Mathew, Mezić & Petzold 2005). In this study, we choose the line element $\mathscr{L}_0 = \{(X_1, X_3)|X_3 = 0, -100 \leqslant X_1 \leqslant -40\}$, and compute its corresponding finite-time largest Lyapunov exponent, σ_{max}, following the procedure of Chabreyrie, Chandre & Aubry (2011). A positive Lyapunov exponent implies chaos and exponential divergence of neighbouring tracers that lie on $\mathscr{L}_0$. To compute Lyapunov exponents
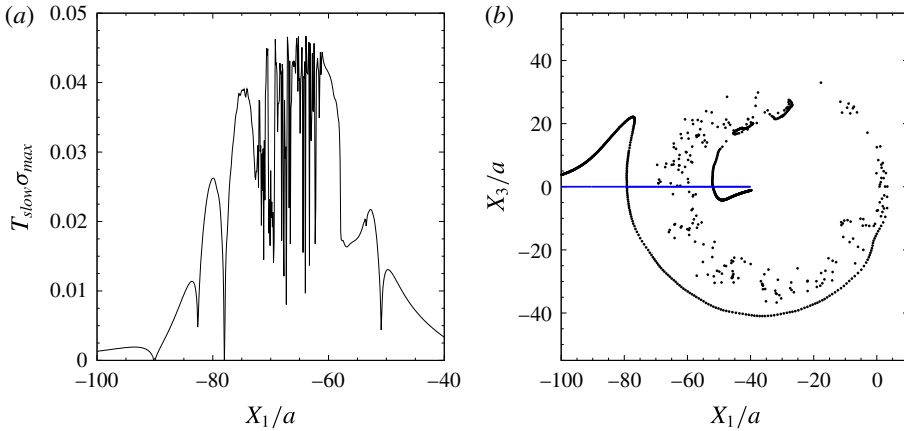
FIGURE 6. (Colour online) (a) The profile of $T_{slow}\sigma_{max}(\mathcal{L}_0, 50T_{slow})$ along the line element $\mathcal{L}_0$. (b) The state of the line element represented by 1000 tracer particles at $t = 0$ (blue solid line) and $t = 50T_{slow}$ (black dots). The element has been disrupted along the path of the swimmer (cf. figure 4a).

corresponding to a particle initially located at $X_0 = X(0)$, we integrate

$$\frac{\mathrm{d}\boldsymbol{\Phi}}{\mathrm{d}t} = \boldsymbol{J}(X(t), t) \cdot \boldsymbol{\Phi}, \quad \boldsymbol{J} = \frac{\partial \boldsymbol{u}}{\partial \boldsymbol{X}}, \quad \boldsymbol{\Phi}(0) = \boldsymbol{I}, \quad\quad (4.1a\text{–}c)$$

along with (2.21) and compute the 3×3 state transition matrix $\boldsymbol{\Phi}(t)$ and its three eigenvalues λ_k ($k = 1, 2, 3$) at $t = T = 50T_{slow}$. The largest Lyapunov exponent is calculated from $\sigma_{max} = T^{-1}max(\lambda_1, \lambda_2, \lambda_3)$. Figure 6(a) shows the variation of $T_{slow}\sigma_{max}(\mathcal{L}_0, T)$. Results do not considerably change by increasing T. We have also shown the deformed and disrupted state of $\mathcal{L}_0$ at $t = T$. Our numerical experiments show that σ_{max} is positive wherever the line element is stretched, and becomes minimum at the tips of the deformed lobes where tracer particles move together and the line element experiences the least stretching and maximum folding. The magnitude of the Lyapunov exponent is small because the swimmer spends a large fraction of time far from a test tracer: a quasi-periodic orbit is characterised by a short period needed to complete a full multi-loop tun and a subsequent long-range stroke, and a long period associated with its orbital precession. During each swimmer–tracer encounter, tracer particles are displaced but they remain almost stationary until the swimmer revisits that part of the configuration space. Since the precession rate of quasi-periodic orbits is $\varpi \sim O(T_{slow}^{-1})$, the recurrence time for swimmer–tracer interaction is $\sim 2\pi/\varpi$, which is long. Therefore, Lyapunov exponents are scaled by T_{slow}^{-1}, and remain almost zero over the hibernation (stationary) phase of tracer particles. These two effects decrease the magnitude of σ_{max} and increase the time scale of mixing substantially. The mixing speed can be enhanced using more swimmers on a given orbit, but hydrodynamic interactions between swimmers must be taken into account.

We have repeated our simulations for different choices of the frequency shift $\Delta\nu$. Our numerical experiments show that chaotic mixing occurs within the invariant torus of all quasi-periodic orbits, and the thickness of the chaotic layer correlates with the structure of the turning loops: the higher the number of loops in a turning
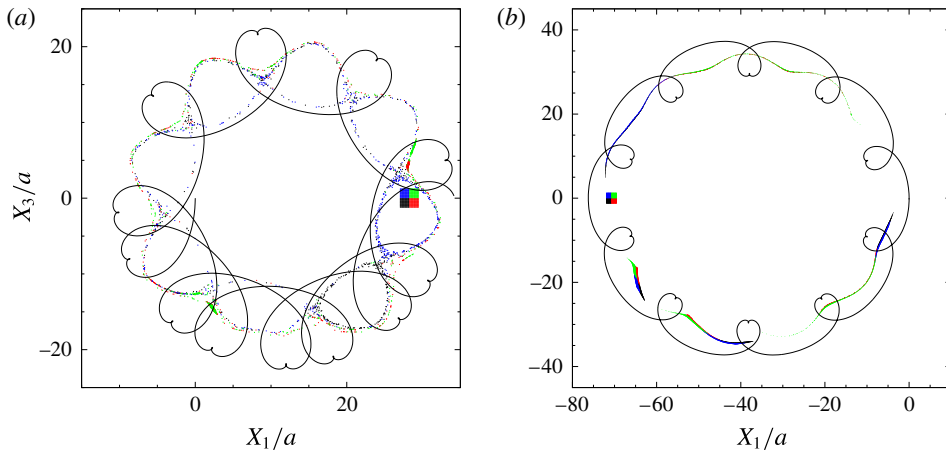
FIGURE 7. (Colour online) (*a*) The quasi-periodic orbit of the swimmer with a single turning cardioid for $\Delta v = 0.00625$, and the dispersed chain-like pattern of tracer packets whose advection starts from the tiled elements at $t = 0$. The snapshot of the chain-like chaotic pattern has been taken at $t = 625 T_{slow}$. The chain-like pattern is rotating. (*b*) The swimmer's periodic orbit with inverted cardioids for $\Delta v = 0.005$. Fluid elements are stretched and transported, without chaos, on a curved path along the periphery of the orbit. The snapshots of the four deforming fluid elements have been taken at $t = 0$, $50 T_{slow}$, $100 T_{slow}$, $200 T_{slow}$, and $400 T_{slow}$.

multi-loop bundle, the greater the number of foldings that a test patch experiences, and consequently the wider the chaotic layer. The number of loops nonlinearly depends on the geometric parameters of the swimmer and Δv. The turning loop of the simplest quasi-periodic orbit in our library is a cardioid corresponding to $\Delta v = 0.00625$ (figure 7*a*). For this swimming mode, the chaotic set forms a rotating chain-like structure in the configuration space. We have not observed any sign of chaos for periodic orbits. For $\Delta v = 0.005$, the swimmer's orbit is periodic with inverted single cardioids as turning loops (figure 7*b*). It is seen that fluid elements are stretched and carried by the swimmer on a curved path, but they are not subject to successive foldings and do not diffuse in the annular region covered by the swimmer's orbit. Full exploration of chaotic zone in the parameter space is the topic of our future research.

5. Conclusions

We have shown that the Quadroar swimmer performs a hybrid pusher and puller swimming like *C. reinhardtii* (Guasto *et al.* 2010; Klindt & Friedrich 2015). To the best of our knowledge, the Quadroar is the only artificial swimmer that induces flow streamlines similar to living flagellar microorganisms. This similarity opens a new ground for understanding the behaviour of bacterial colonies, and the way that they influence their environmental fluid and redistribute nutrients/chemicals. One of the interesting subjects in biology is to understand social interactions between the members of animal groups. The complexity of such interactions increases for living beings with advanced neural and sensory systems. For simple swimming microorganisms, interactions have hydrodynamic origin while individuals perform chemotaxis. Given the similarities between the flow field induced by the Quadroar

and flagellar swimmers, we have now the machinery to develop more realistic models of hydrodynamic interactions between microorganisms and simulate their collective swarms.

We have demonstrated that a Quadroar swimmer can chaotically mix its surrounding fluid over the area that the swimmer's quasi-periodic trajectory covers. The advantage of this mixing strategy is highlighted particularly where the fluid is quiescent, or if it flows sufficiently slow that mixing based on the channel wall corrugations is inefficacious. Microswimmer-induced chaotic mixing may be used to revitalise marine life in the dead zones of the oceans and estuaries where the shortage of microorganisms and their stirring contribution (cf. Katija 2012; Wilhelmus & Dabiri 2014) has negatively impacted the ecological cycle. The behaviour of a single Quadroar in the presence of solid boundaries, i.e. walls, and whether its quasi-periodic orbit is retained remains to be investigated. Of particular interest is the special case of the swimmer inside a fully confined space (a chamber), and whether a uniform mixing over the entire space can be achieved. A swarm of Quadroars is expected to achieve a spatially uniform mixing with a much higher efficiency and larger Lyapunov exponents, details of which requires several computational challenges to be overcome and shall be addressed in a separate study.

Acknowledgements

REFERENCES

AREF, H. 1991 Stochastic particle motion in laminar flows. *Phys. Fluids* A **3** (5), 1009–1016.

CHABREYRIE, R., CHANDRE, C. & AUBRY, N. 2011 Complete chaotic mixing in an electro–osmotic flow by destabilization of key periodic pathlines. *Phys. Fluids* **23**, 072002.

COUCHMAN, I. J. & KERRIGAN, E. C. 2010 Control of mixing in a Stokes' fluid flow. *J. Process Control* **20**, 1103–1115.

ECKHARDT, B. & ZAMMERT, S. 2012 Non-normal tracer diffusion from stirring by swimming microorganisms. *Eur. Phys. J.* E **35** (96), 1–2.

ELGETI, J., WINKLER, R. G. & GOMPPER, G. 2015 Physics of microswimmers—single particle motion and collective behaviour: a review. *Rep. Prog. Phys.* **78**, 056601.

FEHLBERG, E. 1968. Classical fifth-, sixth-, seventh-, and eighth-order Runge–Kutta formulas with stepsize control. Technical Report, 287. National Aeronautics and Space Administration.

GOUILLART, E., KUNCIO, N., DAUCHOT, O., DUBRULLE, B., ROUX, S. & THIFFEAULT, J. L. 2007 Walls inhibit chaotic mixing. *Phys. Rev. Lett.* **99**, 114501.

GOUILLART, E., DAUCHOT, O., DUBRULLE, B., ROUX, S. & THIFFEAULT, J. L. 2008 Slow decay of concentration variance due to no-slip walls in chaotic mixing. *Phys. Rev.* E **78**, 026211.

GUASTO, J. S., JOHNSON, K. A. & GOLLUB, J. P. 2010 Oscillatory flows induced by microorganisms swimming in two dimensions. *Phys. Rev. Lett.* **105**, 168102.

HAPPEL, J. & BRENNER, H. 1983 *Low Reynolds Number Hydrodynamics*. Martinus Nijhoff Publishers.

JALALI, M. A., ALAM, M.-R. & MOUSAVI, S. 2014 Versatile low-Reynolds-number swimmer with three dimensional maneuverability. *Phys. Rev.* E **90**, 053006.

KATIJA, K. 2012 Biogenic inputs to ocean mixing. *J. Expl Biol.* **215**, 1040–1049.

KLINDT, G. S. & FRIEDRICH, B. M. 2015. Flagellar swimmers oscillate between pusher- and puller-type swimming. arXiv:1504.05775v1.

LIN, Z., THIFFEAULT, J.-L. & CHILDRESS, S. 2011 Stirring by squirmers. *J. Fluid Mech.* **669**, 167–177.

LIU, R. H., SHARP, K. V., OLSEN, M. G., STREMLER, M. A., SANTIAGO, J. G., ADRIAN, R. J. & BEEBE, D. J. 2000 A passive three-dimensional 'C-shape' helical micromixer. *J. Microelectromech. Syst.* **9**, 190–198.

LOPEZ, D. & LAUGA, E. 2014 Dynamics of swimming bacteria at complex interfaces. *Phys. Fluids* **26**, 071902.

MATHEW, G., MEZIĆ, I. & PETZOLD, L. 2005 A multiscale measure for mixing. *Physica* D **211**, 23–46.

MATHEW, G., MEZIĆ, I., GRIVOPOULOS, S., VAIDYA, U. & PETZOLD, L. 2007 Optimal control of mixing in Stokes fluid flows. *J. Fluid Mech.* **580**, 261–281.

NIENOW, A. W., EDWARDS, M. F. & HARNBY, N. 1997 *Mixing in the Process Industries*. Butterworth-Heinemann.

OTTINO, J. M. 1989 *The Kinematics of Mixing: Stretching, Chaos, and Transport*. vol. 3. Cambridge University Press.

OTTINO, J. M. 1990 Mixing, chaotic advection, and turbulence. *Annu. Rev. Fluid Mech.* **22**, 207–254.

OTTINO, J. M. & WIGGINS, S. 2004 Introduction: mixing in microfluidics. *Phil. Trans. R. Soc. Lond.* A **362**, 923–935.

PAK, O. S. & LAUGA, E. 2015 Theoretical models in low Reynolds number locomotion. In *Fluid–Structure Interactions in Low Reynolds Number Flows* (ed. C. Duprat & H. A. Stone), RSC Publishing.

PUSHKIN, D. O. & YEOMANS, J. M. 2013 Fluid mixing by curved trajectories of microswimmers. *Phys. Rev. Lett.* **111**, 188101.

RAUWENDAAL, C. (Ed.) 1991 *Mixing in Polymer Processing*. vol. 23. CRC Press.

STROOCK, A. D., DERTINGER, S. K. W., AJDARI, A., MEZIĆ, I., STONE, H. A. & WHITESIDES, G. M. 2002 Chaotic mixer for microchannels. *Science* **295**, 647–651.

STURMAN, R. & SPRINGHAM, J. 2013 Rate of chaotic mixing and boundary behavior. *Phys. Rev.* E **87**, 012906.

THIFFEAULT, J. L., GOUILLART, E. & DAUCHOT, O. 2011 Moving walls accelerate mixing. *Phys. Rev.* E **84**, 036313.

WU, X.-L. & LIBCHABER, A. 2000 Particle diffusion in a quasi-two-dimensional bacterial bath. *Phys. Rev. Lett.* **84**, 3017–3020.

WAGNER, G. L., YOUNG, W. R. & LAUGA, E. 2014 Mixing by microorganisms in stratified fluids. *J. Mar. Res.* **72**, 47–72.

WIGGINS, S. & OTTINO, J. M. 2004 Foundations of chaotic mixing. *Phil. Trans. R. Soc. Lond.* A **362**, 937–970.

WILHELMUS, M. M. & DABIRI, J. O. 2014 Observations of large-scale fluid transport by laser-guided plankton aggregations. *Phys. Fluids* **26**, 101302.